Crystal Structure of Farnesyl Protein Transferase Complexed with a CaaX Peptide and Farnesyl Diphosphate Analogue[†]

Corey L. Strickland, William T. Windsor, Rosalinda Syto, Lynn Wang, Richard Bond, Zhen Wu, Jeffrey Schwartz, Hung V. Le, Lorena S. Beese,[‡] and Patricia C. Weber*

Structural Chemistry and Tumor Biology Departments, Schering-Plough Research Institute, 2015 Galloping Hill Road, K15-3-3855, Kenilworth, New Jersey 07033-0539, and Department of Biochemistry, Duke University Medical Center, Durham, North Carolina 27710

ABSTRACT: The crystallographic structure of acetyl-Cys-Val-Ile-selenoMet-COOH and α-hydroxyfarnesylphosphonic acid (αHFP) complexed with rat farnesyl protein transferase (FPT) (space group $P6_1$, $a = b = 174.13$ Å, $c = 69.71$ Å, $\alpha = \beta = 90°$, $\gamma = 120°$, $R_{factor} = 21.8\%$, $R_{free} = 29.2\%$, 2.5 Å resolution) is reported. In the ternary complex, the bound substrates are within van der Waals contact of each other and the FPT enzyme. αHFP binds in an extended conformation in the active-site cavity where positively charged side chains and solvent molecules interact with the phosphate moiety and aromatic side chains pack adjacent to the isoprenoid chain. The backbone of the bound CaaX peptide adopts an extended conformation, and the side chains interact with both FPT and αHFP. The cysteine sulfur of the bound peptide coordinates the active-site zinc. Overall, peptide binding and recognition appear to be dominated by side-chain interactions. Comparison of the structures of the ternary complex and unliganded FPT [Park, H., Boduluri, S., Moomaw, J., Casey, P., and Beese, L. (1997) *Science 275*, 1800−1804] shows that major rearrangements of several active site side chains occur upon substrate binding.

Posttranslational modification of proteins by prenylation is one mechanism of cellular regulation. Of immediate relevance to the treatment of cancer is farnesylation of the monomeric G protein, p21 Ras, which plays a central role in the regulation of cellular proliferation, differentiation, and apoptosis (*1, 2*). Expression of mutant forms of Ras correlates with cellular transformation and tumor development. Nearly 30% of all human cancers contain oncogenic forms of Ras, with an extraordinarily high prevalence in selected cancer tissues such as pancreatic (90%), colorectal (50%), and lung (40%) (*3*). Both the regulated and unregulated oncogenic transforming activities of Ras require its physical association with the proximal side of the plasma membrane (*4*). Part of the membrane localization mechanism involves addition of a hydrophobic isoprenoid unit to a cysteine residue near the carboxyl-terminus of Ras. This posttranslational modification is catalyzed by farnesyl protein transferase (FPT). Inhibitors of FPT block incorporation of farnesyl diphosphate (FPP, **1**) into Ras and cause reversion of Ras transformed cells (*5*). Consequently, the development of potent and specific inhibitors of FPT is an emerging, mechanism-based strategy for blocking cellular transformation and tumor growth.

FPT-mediated prenylation of Ras involves formation of a ternary FPT:FPP:Ras complex, followed by transfer of the 15 carbon isoprenoid from FPP to a cysteine side chain of Ras. The cysteine residue is part of a conserved carboxyl terminal Ca_1a_2X sequence where X is a serine residue in H-Ras and methionine in N-Ras, K-Ras 4a, and K-Ras 4b isoforms. In other protein and peptide substrates of FPT, the terminal residue of the Ca_1a_2X sequence can be cysteine, alanine, or glutamine (*6*). Studies using synthetic peptide libraries incorporating both natural and unnatural amino acids have shown that a variety of amino acids can be accommodated at the a_1 position without loss of reactivity (*6*). Peptides having small apolar residues at a_2 are also good substrates, while those with aromatic side chains at this position competitively inhibit binding of peptide substrates (*7*). For example, CVFM-COOH competitively inhibits FPT binding of ras-derived peptides such as Biotin-KTKSKCVIM-COOH [$K_i = 35$ nM (*6*)]. Screening of synthetic peptide libraries also lead to discovery of inhibitors competitive with FPP. These include D-tryptophan-D-methionine-D-4-chlorophenylalanine-L-γ-carboxyglutamic acid which binds FPT with high affinity ($K_d = 2$ nM) (*8*). Several nonhydrolyzable FPP analogues, such as α-hydroxyfarnesylphosphonic acid (**2**, αHFP, $K_i = 5$ nM) and [[(farnesylmethyl)hydroxyphosphinyl]methyl]phosphonic acid (farnesyl-PMP, $K_i = 830$ nM) (*9*), also inhibit FPT.

Farnesyl diphosphate (1)

α-Hydroxyfarnesylphosphonic acid (2)
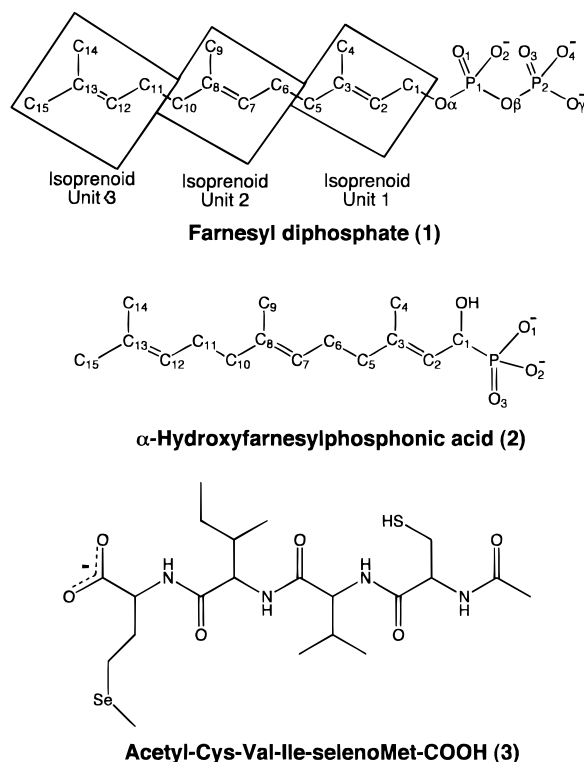

Acetyl-Cys-Val-Ile-selenoMet-COOH (3)

FIGURE 1: Chemical structures of FPT substrates and inhibitors.

FPT performs an ordered sequential reaction where formation of the FPT:FPP complex precedes binding of the Ca_1a_2X substrate (*10*). In fact, a dead-end complex forms if the Ca_1a_2X sequence binds first (*11*). Product formation is relatively fast ($\sim0.8-12$ s^{-1}), and the rate-limiting step is product release (0.06 s^{-1}) (*11*). While a zinc ion is required for catalysis (*12*), the chemical mechanism of farnesyl transfer is poorly understood. A mechanism involving nucleophilic attack of the FPP by an activated cysteine thiol is supported by recent spectroscopic results which indicate that the cysteine side chain of the Ca_1a_2X sequence coordinates the FPT catalytic zinc (*13*). Alternatively, analyses of the product stereochemistry and effects of FPP analogues have suggested that development of a carbocation on the C1 atom of FPP leads to electrophilic alkylation of the cysteine sulfur to form the thioether bond (*14–16*).

Structural studies of FPT:substrate complexes were undertaken to investigate the chemical events involved in farnesyl transfer. This information, along with knowledge of the substrate-binding modes, will be useful in the design and synthesis of substrate analogues and mechanism-based FPT inhibitors. Here, we report the structure of FPT complexed with a tetrapeptide substrate (7), acetyl-Cys-Val-Ile-selenoMet-COOH (**3**, CVIM, Figure 1), and α-hydroxyfarnesylphosphonic acid (**2**, αHFP, Figure 1), an unreactive FPP analogue. Comparison of this structure, the first of an FPT:substrate ternary complex, with that of unliganded rat FPT (*17*) reveals both global and local conformational changes accompanying substrate binding. Structural features of the ternary complex, in particular the short distance (2.5 Å) between the cysteine sulfur of the peptide and FPT active-site zinc, suggest participation of an activated thiol in the catalytic mechanism. In the structure, however, the FPP C1 carbon and peptide cysteine sulfur are 7 Å apart. For direct farnesyl transfer, some movement of the substrates from the

positions observed in this structure is expected. Clearly, the first structure of FPT complexed with a peptide substrate and FPP analogue has provided the initial indications of dynamic processes associated with substrate binding and the enzymatic reaction itself. These, and elements of the ternary complex important for understanding recognition of Ras proteins by FPT, are discussed in detail.

EXPERIMENTAL PROCEDURES

Protein Purification and Crystallization. Rattus norvegicus farnesyl protein transferase was expressed, purified, and assayed as previously described for human FPT (*18*). Human FPT is 93 and 97% identical to rat FPT in the α- and β-subunits, respectively. Purified FPT was dialyzed against 20 mM Tris, pH 7.7, 1 mM DTT, 20 mM KCl, and 10 μM ZnCl$_2$ and concentrated to 0.27 mM (25 mg/mL) prior to crystallization. The Ac-Cys-Val-Ile-selenoMet-COOH: αHFP:FPT ternary complex was prepared by incubating 108 μM FPT (10 mg/mL) with 300 μM αHFP (Calbiochem-Novabiochem Corporation) for 2 h prior to adding 300 μM Ac-Cys-Val-Ile-Met(Se)-COOH (AnaSpec Inc.). αHFP was added from a 23.6 mM solution in ethanol, yielding 0.6% (v/v) ethanol in the final solution. The peptide was added from a 50 mM solution in DMSO, resulting in a 0.3% (v/v) final DMSO concentration. The ternary mixture was incubated at 4 °C for an additional 4.5 h.

Vapor diffusion crystallization experiments were conducted using the hanging drop method. Potential crystallization conditions were screened by sparse matrix sampling (*19*) and systematic grid screens (*20*) using standard solutions (Hampton Research Inc.). Crystals suitable for structure determination grew when the droplet contained 4 μL of the αHFP:peptide:FPT complex, 4 μL of the reservoir solution (7% PEG 4000, 0.1 M sodium acetate, pH 5.7), and 1 μL of 200 mM DTT. Crystallization trays were incubated at 22 °C, and after 2–3 weeks, hexagonal rods (0.1 mm × 0.3 mm) appeared. Prior to data collection, crystals were taken directly from the crystallization droplet and flash frozen in liquid propane using a cryoprotectant consisting of the reservoir solution supplemented with 25% (v/v) glycerol. Crystals belong to space group $P6_1$ with unit cell parameters $a = b = 174.13$ Å, $c = 69.71$ Å, $\alpha = \beta = 90°$, and $\gamma = 120°$ and diffract to 2.4 Å resolution. The crystals described here are distinct from those of unliganded FPT which grow in the absence of substrates or substrate analogues. The unliganded FPT crystals belong to a different space group ($P6_5$, $a = b = 167.1$ Å, $c = 97.9$ Å, $\alpha = \beta = 90°$, $\gamma = 120°$) and form using alternate solution conditions and pH (14% PEG 8000 and 0.2 M ammonium acetate at pH 7.0) (*17*).

Data Collection. Data were collected using a Raxis-IIc image plate area detector mounted on a Rigaku-R200 rotating anode X-ray generator operating at 50 kV and 100 mA. X-ray intensity at the crystal was increased by focusing with "bent mirrors" (J. Johnson and Dr. Z. Otwinowski, Yale University; Molecular Structure Corp.). With the detector set at $2\theta = 0°$ and a crystal-to-detector distance of 135 mm, data were collected in 180 contiguous 0.30° oscillation images each exposed for 12 min. Diffraction images were reduced to integrated intensities using HKL (*21*). Data quality statistics are shown in Table 1.

Table 1: Summary of Crystallographic Parameters

Data Statistics		
resolution (Å)		15.0−2.4
reflections (measured/unique)		144 714 (42 739)
completeness (overall/outer shell) (%)		90 (57)
$R_{sym}{}^a$ (overall/outer shell) (%)		6.1 (37)
$|I/\sigma_I|$ (overall/outer shell)		20.0 (3.0)
Refinement Statistics		
residues modeled	no. of atoms	avg *B*-factor
α (54−366)	2665	43.0^b
β (523−923)	3154	40.0^b
solvent	248	44.8^c
zinc	1	31.4
αHFP	21	25.2^c
Ac-CVIM(Se)	30	35.8^b
R_{factor} $(R_{free})^d$ 8.0−2.4 Å		21.8% (29.2%)

^{a} $R_{sym} = \sum(ABS(I − \langle I \rangle))/\sum(I)$. ^{b} Backbone atoms used for *B*-factor average. ^{c} All non-hydrogen atoms used for *B*-factor average. ^{d} 5% of data were excluded from the refinement to calculate R_{free}.

Structure Determination and Refinement. The structure of αHFP and CVIM complexed with FPT was solved by molecular replacement, as implemented in XPLOR (*22*). The 2.25 Å resolution structure of unliganded FPT (*17*) was used as the search model. The rotation function calculated over the resolution range 15−4.0 Å yielded a peak 4.1σ above the mean at τ1 = 26.6°, τ2 = 27.5°, and τ3 = 14.6°. Patterson correlation refinement (*23*) of this rotation function solution gave a value of 0.129, significantly above the next highest peak. In a translation search from 15.0 to 4.0 Å resolution, $P6_1$ proved to be the correct space group as evidenced by a 32σ peak at fractional coordinates *x* = 0.79 and *y* = 0.52. The initial *R*-factor incorporating data from 15.0 to 4.0 Å after rigid body refinement was 0.35.

Several cycles of model building and refinement by both simulated annealing and positional methods were carried out to accommodate structural changes due to crystallization of the protein in a different space group and to binding of the substrates. Positions of discrete water molecules were taken from positive 3σ $(F_o − F_c),\alpha_{calc}$ difference density peaks if a hydrogen-bonding pattern to protein, peptide, or other solvent molecules could be established. The peptide and αHFP were added after several rounds of refinement, although density for these groups was a prominent feature even in the initial electron density map. Density for the entire peptide was continuous, and the location of the Se atom of the selenoMet residue clearly defined by a >20σ peak in the $(F_o − F_c),\alpha_{calc}$ map (Figure 2b).

Density for the αHFP phosphate and isoprenoid chain was unambiguous, although density for the α-hydroxyl group was weak (Figure 2a). αHFP was purchased as a racemic mixture and weaker density was attributed to binding of both stereoisomers. Given the mixture of stereoisomers at C1 (Figure 1), hydroxyl groups at positions corresponding to both the R and S chiralities at C1 were included in the model. Following refinement, the electron density at the position of each hydroxyl oxygen indicated a strong preference for the S chirality, i.e., the hydroxyl group position corresponding to the S configuration gave a $(2F_o − F_c),\alpha_{calc}$ value of 0.9σ, while the hydroxyl group position corresponding to the R configuration resulted in a lower $(2F_o − F_c),\alpha_{calc}$ value of 0.1σ. The stereochemical preference appears to arise from elimination of sterically unfavorable contacts with atoms of the protein interior and a preferred orientation of the hydroxyl
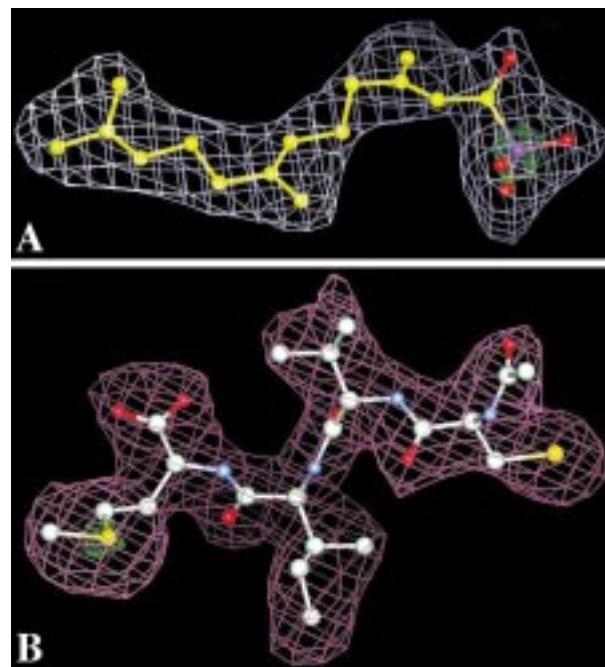

FIGURE 2: Electron density maps. An omit electron density map was calculated using the final refined model with αHFP and CVIM removed. (a) αHFP omit $(F_o − F_c),\alpha_{calc}$ electron density at +2.7σ (white) and +12σ (green). (b) CVIM omit $(F_o − F_c),\alpha_{calc}$ electron density at +2.7σ (purple) and +25σ (green).

group toward solvent where hydrogen bonding with water molecules occurs. For this reason, a model of αHFP having S chirality at the C1 position was used in the final stages of refinement.

Alternate cycles of refinement and model building were conducted until no interpretable positive or negative peaks greater than ±5σ appeared in the difference density maps. Residues 54−366 of the α-subunit and residues 23−423 of the β-subunit show continuous, well-defined electron density and are included in the final model. The waters are rank ordered by the $(2F_o − F_c),\alpha_{calc}$ electron density calculated at the position of each oxygen. Using this system, water molecules which are more highly ordered are given lower sequence numbers. Electron density maps were inspected, and the model was fit using the graphics display program CHAIN (*24*). Bond distance and angle parameters for αHFP were calculated using Quanta (Molecular Simulations Inc.). No explicit zinc-to-ligand restraints were used in the refinement. Available data to 2.4 Å resolution were included in the crystallographic refinement. Given the extent of missing data in the 2.5−2.4 Å higher resolution shell (60%), the nominal resolution of the structure is closer to 2.5 Å resolution. Statistics of the final model are given in Table 1.

Structural Analysis. Structural superpositions were carried out using an overlay strategy described by Chothia and Lesk [HOMOLOGCORE, (*25*)]. Overlays included only the equivalent α-carbons in helices within a 2 Å cutoff and rms difference calculations excluded deviations greater than 3.0 Å. Surface area calculations and modeling were accomplished using INSIGHT (Molecular Simulations Inc.). A probe of 1.4 Å radius, corresponding to a water molecule, was used in the surface area calculations. Figures were generated using MOLSCRIPT (*26*), RASTER3D (*27*), INSIGHT, GRASP (*28*), and CHAIN (*24*).
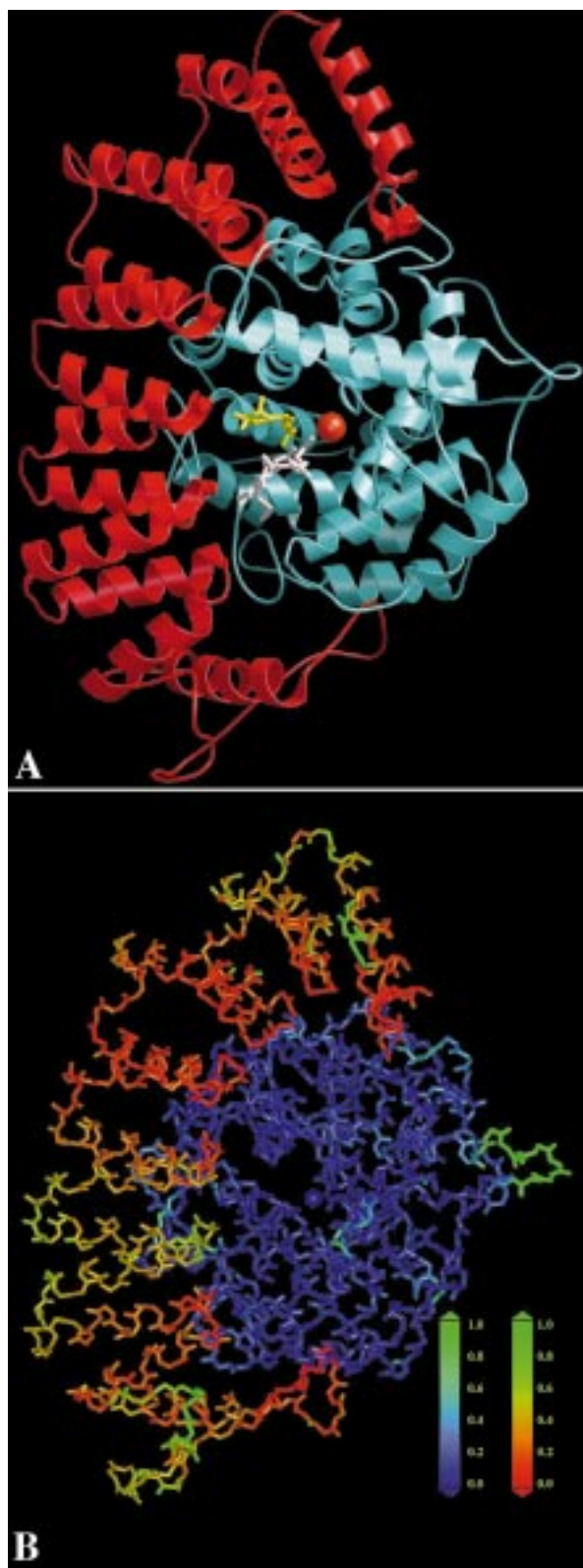
FIGURE 3: Overall structure of FPT. (a) Ribbon representation showing the α-subunit (red) and β-subunit (blue). Bound to FPT are the zinc (orange sphere), αHFP (yellow) and the CVIM peptide (white). (b) Global conformational differences between the unliganded FPT (*17*) and the FPT:αHFP:CVIM complex. Backbone atoms are colored by the difference in position between the two structures. The α-subunit mainchain atoms are colored from red to green corresponding to 0 to >1.0 Å differences. The β-subunit residues are colored from blue to green corresponding to 0 to >1.0 Å differences.

RESULTS

Overall Structure. Many features present in the unliganded farnesyl protein transferase structure (*17*) are retained in the ternary complex. Both subunits are organized about α-helical secondary structures (Figure 3a). The 378 residue α-subunit is composed of seven pairs of antiparallel α-helices folded into a crescent. The 438 residue β-subunit forms an unusual two layer α-helical barrel. Subunit association produces a prominent active-site cavity lined with side chains from both subunits. In the ternary complex and unliganded structure, Asp297β, Cys299β, and His362β side chains ligate the active-site zinc. No differences greater than the experimental coordinate error are observed in the ligand side-chain-to-zinc distances of the two structures.

Despite preservation of secondary structure, global conformational differences in the unliganded and complexed structures are observed. Superposition of the structures shows that the major structural alterations occur in the α-subunit, while the spatial arrangement of helices in the β-subunit is unchanged (Figure 3b). The 179 α-carbons within the 14 helices of the β-subunit superimpose with an rms deviation of 0.35 Å, a value within the estimated coordinate error. In contrast, 195 α-carbons in the 15 α-subunit helices superimpose with an rms deviation of 0.67 Å. Structural changes in the α-subunit involve relative translations of the helices. These shifts are unevenly distributed over the α-subunit. Helices 8a and 9a, as defined by Park et. al. (*17*), shift ~0.3 Å, while helices 4a, 5a, 12a, and 14a show shifts approaching 1 Å (Figure 3b). Movement of helices 4a (residues 148−161) and 5a (residues 166−179) are particularly important since they are located near the active site. For example, Tyr166α, located at the start of helix 5a, is translated ~1.2 Å. Overall, the helix translations do not significantly alter the active-site volume.

In addition to global changes, several side chains in the active site undergo major conformational changes on substrate binding (Figure 4a). In the unliganded structure, Arg202β makes few direct interactions with other FPT groups (Figure 4b). Similarly, the Tyr166α side chain is oriented toward solvent and makes a weak 3.7 Å hydrogen bond to the backbone nitrogen of Glu198β. The Glu198β side-chain is also oriented away from the active site and interacts with a network of ordered water molecules. Lack of strong, directional bonding by Arg202β and Tyr166α side chains is reflected in their side chain *B*-values which, in the unliganded structure, are the highest among the active-site residues. On substrate binding, these residues rearrange, participate in several hydrogen bond networks, and consequently become more ordered as evidenced by a decrease in the atomic *B*-factors (Figure 4c). In the FPT:substrate complex, the third isoprenoid unit of αHFP has displaced Arg202β. The Arg side chain has rotated ~90° about χ_1 resulting in a 6.8 Å movement of the guanidinium group, which now forms a bidentate ion pair with Asp200β. The side chain of Tyr166α, located at the start of helix 5a, undergoes an ~110° rotation about χ_1. The aromatic ring stacks parallel to the guanidinium group of Arg202β and forms an edge-to-face interaction with the His201α imidazole. The Tyr166α hydroxyl group forms a 2.9 Å hydrogen bond with the Tyr251β hydroxyl. Movements in the Glu198β side chain result from rotations of 50° about Φ
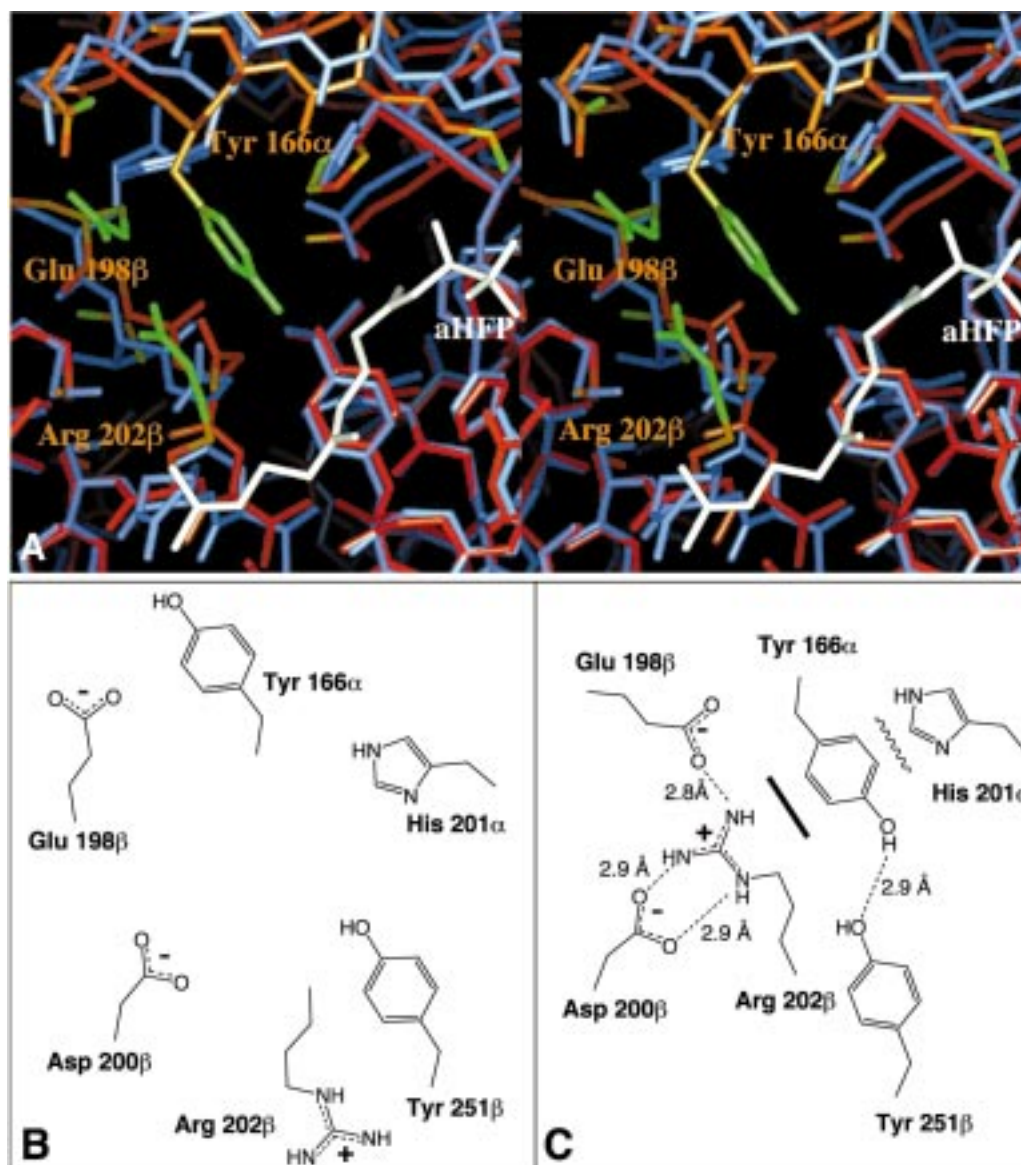
FIGURE 4: Structural changes on substrate binding. (a) Stereoscopic representation of the active site region of FPT following superposition of the unliganded structure (17) and ternary complex. The unliganded structure is colored blue. The ternary complex is colored from red to green corresponding to 0 to 4.0 Å shifts in atomic position. (b) Schematic diagram of the unliganded FPT active site. (c) Schematic diagram of side-chain interactions in the ternary complex. The solid bar represents a stacking of Arg202β with Tyr166α. The curlicue represents an edge-to-face interaction of Tyr166α and His201β.

and 130° about χ_1. In the ternary complex, the Glu198β side-chain carboxylate is bonded to the Arg202β guanidinium group. Overall, a single, weak protein-to-protein hydrogen bond is lost, and six new interactions result from the substrate-induced side-chain rearrangements.

FPT-αHFP and FPT−FPP Interactions. In the ternary complex, αHFP binds in an extended conformation along one side of the large active-site cavity (Figure 3a). αHFP is essentially sequestered from solvent with 500 Å^2 of the total 550 Å^2 molecular surface area buried. Seventeen FPT residues contact 440 Å^2 of the molecular surface, while side chains of the CVIM peptide contact 60 Å^2.

The farnesyl chain is directed toward the molecular interior and interacts primarily with aromatic residues (Figure 5a). The isoprenoid units become increasingly well-ordered with distance from the molecular surface, as evidenced by the decrease in atomic *B*-factors along the farnesyl chain (~40 Å^2 at C1 decreasing to ~20 Å^2 at C15). The first isoprene

unit (C$_1$−C$_5$) binds in an aromatic pocket formed by Tyr251β, Tyr166α, Tyr200α, His248β, and His201α. The second isoprenoid unit (C$_6$−C$_{10}$) interacts with the Ile side chain of the peptide, Gly250β and Trp303β. The third unit (C$_{11}$−C$_{15}$) packs against the aliphatic chain of Arg202β and a cluster of aromatic residues including Trp102β, Trp303β, Tyr154β, and Tyr205β. The extensive van der Waals contacts made by the farnesyl chain likely contribute to the high affinity of αHFP for FPT [K_i = 5 nM (9)].

The αHFP phosphate binds in a pocket surrounded by four positively charged side chains and ordered solvent molecules (Figure 5a). Phosphate atom O1 could form 2.7 Å hydrogen bonds with two ordered solvent molecules, Wat 4 and Wat 41 (Figure 6b). However, Arg291β and Lys164α are closer than 3.5 Å and could potentially interact with O1 (Figure 5a). O2 forms hydrogen bonds with His248β and an ordered solvent molecule. O3 makes no direct contacts with FPT, but interacts with two ordered solvent molecules. The
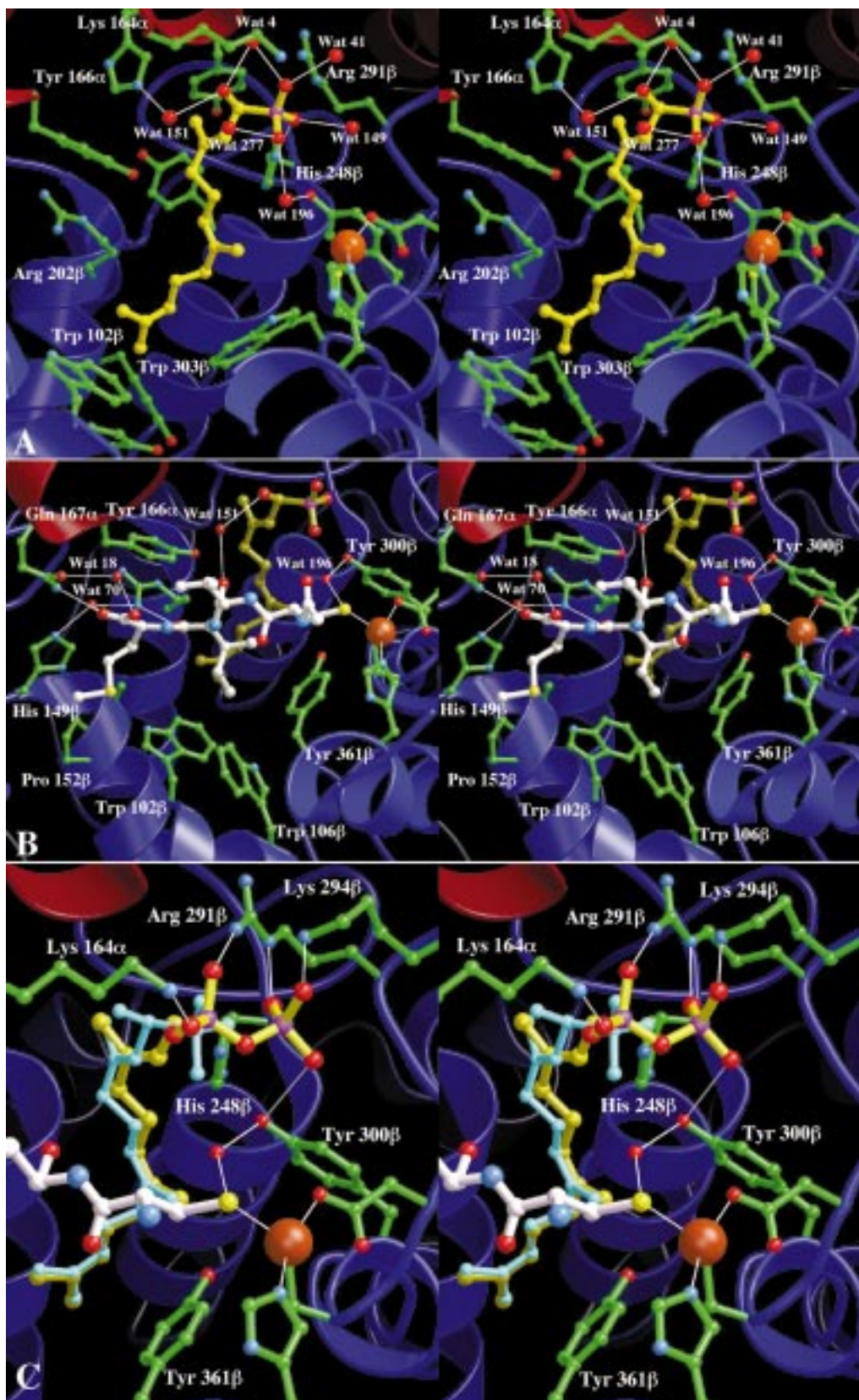
FIGURE 5: Binding of (a) αHFP and (b) CVIM and (c) FPP to FPT. The stereoviews of panels **a** and **b** show the bound αHFP and CVIM peptide in yellow and white, respectively. The zinc is represented as a dark orange sphere. Red and blue ribbons indicate the α- and β-subunits of FPT, respectively. Potential hydrogen bonds are shown by thin white lines. For comparison, the FPP:FPT complex is shown in panel **c** with αHFP superimposed (cyan). The coordinates for the FPT:FPP complex were taken from an independently determined structure at 2.2 Å resolution (unpublished data, C. Strickland) that is similar to the published 3.4 Å structure (*29*).

α-hydroxyl group is directed toward solvent and interacts with several ordered solvent molecules. Overall, the phosphate oxygen-to-protein hydrogen bonds are long (>2.9 Å),

suggesting that although the monophosphate of αHFP can be accommodated in the FPP diphosphate-binding site, the interactions are likely not optimal.
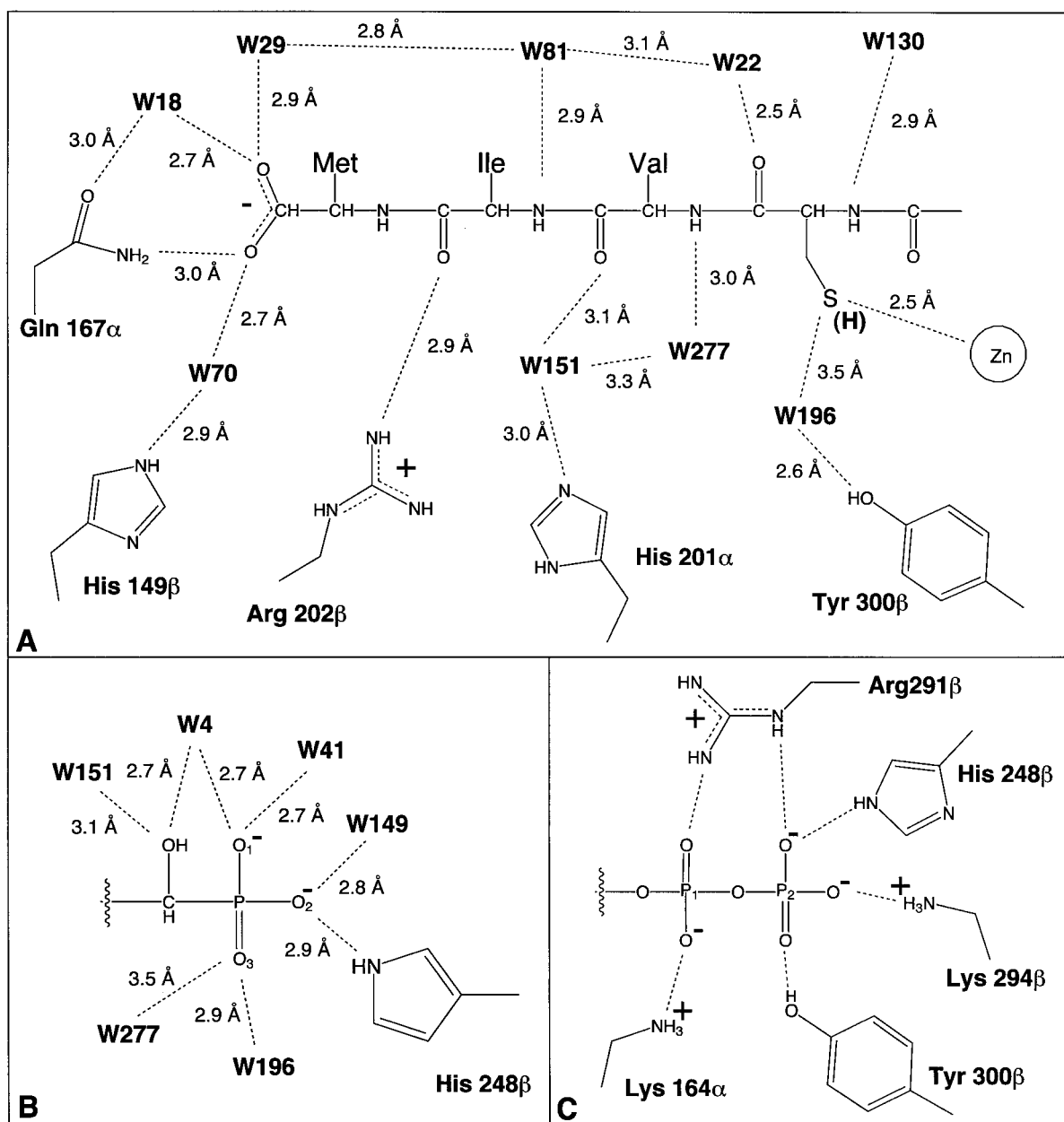
FIGURE 6: Schematic diagrams of interactions of FPT with (a) the CVIM peptide, (b) the αHFP phosphate group, and (c) the FPP diphosphate.

The bound conformation of αHFP resembles that of FPP observed in the low resolution (3.4 Å) structure of the FPT: FPP complex [Figure 5c (29)]. Oxygen atoms of the FPP P1 atom are hydrogen bonded to Arg291β and Lys164α, similar to the interactions observed in the ternary complex (Figures 5c and 6c). O4 interacts with Arg291β and His248β, and O5 and O6 interact with Lys294β and Tyr300β, respectively.

Site-directed mutants of FPT show altered substrate affinity and catalytic activity. In the FPP:FPT complex, the FPP diphosphate forms salt bridges with Arg291β, Lys294β, and Lys164α (Figures 5c and 6c). Mutation of either Arg291β or Lys294β to alanine decreases the affinity of FPT for FPP by about 40-fold (30). While these residues interact directly with FPP, the binding affinity of the peptide also decreases ~7-fold (30). Coupling of decreases in FPP and peptide affinities is consistent with the finding that the substrates are within van der Waals contact in the FPP:peptide:FPT complex. Mutation of Tyr300β, which also interacts with

the pyrophosphate of FPP (Figure 5c and 6c), does not affect the K_m of FPP (30). The 4-fold lower k_{cat} of this mutant suggests a role of Tyr 300β in catalysis (see Discussion).

FPT-CVIM Interactions. The Ac-Cys-Val-Ile-selenoMet-COOH peptide is well-defined in the electron density maps (Figure 2b). The direction of the peptide chain was unambiguously identified using the 22σ positive peak that appeared in the initial difference maps and corresponded to the selenium atom of the selenomethionine. The peptide binds in an extended conformation and spans the large active-site cavity (Figure 3a). The peptide contacts both the FPT enzyme and atoms of FPP (Figure 5b). The peptide main chain interacts directly with FPT through packing of the Ile-to-Met peptide bond adjacent the aromatic ring of Tyr166α, and hydrogen bonding between the Ile carbonyl and the guanidinium group of Arg202β (Figure 5b). Additional peptide main-chain-to-FPT interactions occur through ordered water molecules (Figure 6a). The terminal carboxylic acid participates in hydrogen bonds with Gln167α and
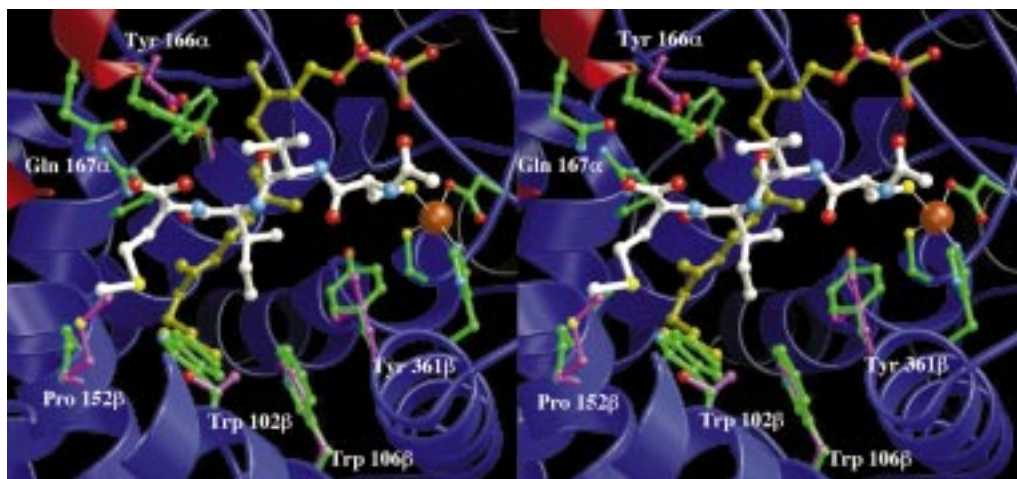
FIGURE 7: Model of FPT:GGPP complex. Residues of FPT are shown in green. Where differences in amino acid sequence occur, the corresponding GGPT residue was modeled and is shown in purple. The sequence label corresponds to FPT. The residues changed are Trp102β to Thr, Trp106β to Phe, Pro152β to Met, Gly241β to Asp, Tyr251β to Ser, and Tyr361β to Leu.

several ordered water molecules (Figures 5b and 6a). The N-terminal acetyl group is oriented toward solvent and makes no direct interactions with FPT.

The larger, hydrophobic side chains of the bound CVIM peptide are oriented toward the interior of the active-site cavity (Figure 5b). Ile, with a 25 Å^2 temperature factor, is the most well-ordered side chain of the bound peptide. The Ile side chain is sequestered in a pocket lined with the side chains of Trp102β, Trp106β, Tyr361β, and the FPP isoprenoid, which buries >90% of its accessible surface area. The Met side chain, also greater than 90% buried, binds in a narrow pocket defined by Trp102β, His149β, Ala151β, and Pro152β. The valine isopropyl group is oriented toward solvent, burying only 37% of the side-chain surface area through packing interactions with Tyr166α. Exposure of the a_1 side chain is consistent with the wide variety of residues accommodated at this position in protein and peptide substrates (6).

The cysteine sulfur of the peptide coordinates the active-site zinc (Figure 5b). Formation of the Cys sulfur-to-zinc coordination involves displacement of a bound solvent molecule which serves as the only nonproteinaceous ligand to the zinc in the substrate-free structure (17). The zinc-to-sulfur distance is 2.5 Å. The separation is longer than the 2.0 Å mean cysteine sulfur-to-zinc distance observed for tetrahedrally coordinated zinc atoms in the protein data bank [~420 examples found (31)] and also longer than the 2.0 Å distance between the zinc atom of FPT and its sulfur ligand provided by the Cys299β side chain. Direct coordination of the cysteine-containing peptide may account for increased ligand−metal charge-transfer bands observed on peptide binding to Co^{2+}-substituted FPT (13). The cysteine sulfur also interacts with Wat 149, which is situated near the C1 carbon of FPP.

DISCUSSION

The ternary complex reported here shows how αHFP and the CVIM tetrapeptide substrate are accommodated in the FPT active site. The structure provides an initial view of the molecular arrangements that accompany substrate binding. The observed mode of peptide recognition via side-chain interactions offers the possibility that the bound conformation of peptide substrates is sequence dependent. Features of the ternary complex suggest that additional conformational changes occur during the catalytic cycle. These points and a model of FPT complexed with FPP and Ras p21, are discussed below.

Catalytic Mechanism. Both electrophilic alkylation and nucleophilic displacement mechanism have been proposed for the farnesylation reaction. Briefly, electrophilic alkylation involves loss of diphosphate to generate a positively charged carbocation on C1 of the farnesyl moiety, which then reacts with the cysteine thiol. Alternatively, a purely nucleophilic displacement reaction would occur via direct attack of an activated cysteine thiol at the C1 carbon of FPP. Product formation by either mechanism results in covalent bond formation between the C1 carbon of FPP and the peptide cysteine sulfur. In this structure, the position of the CVIM peptide results in a separation between these two atoms of about 7 Å. Therefore, independent of the chemical mechanism of the farnesylation reaction, movement of one or both of the substrates from the position(s) observed in this structure is likely.

The coordination of the cysteine sulfur to the zinc supports a direct role of zinc in catalysis. In addition, the structure of the ternary complex helps define other residues potentially involved in catalysis. His248β, Tyr300β, and Tyr361β are close to the FPP C1. Overall, the site-directed mutagenesis experiments and the three-dimensional structure of the FPT ternary complex suggest participation of Tyr300β in the catalytic cycle. The hydroxyl of Tyr300β is within 3.5 Å of the O4 oxygen. Mutation of Tyr300β to Phe reduced k_{cat} ~4-fold relative to the wild-type enzyme (30). Given that product dissociation has been shown to be rate limiting, small changes in the k_{cat} value could potentially mask larger effects on the chemical step of the reaction (11, 32). The importance of Tyr361β has yet to be established. However, a leucine residue occupies this position in the closely related GGPT-I (Figure 7), suggesting that residues at this site may not be critical in the catalytic cycle. While the proximity of the His248β imidazole to the O5 oxygen (3.5 Å) offers the possibility of a direct role in catalysis, mutation of His248β to Ala has little affect on the activity of FPT (30).
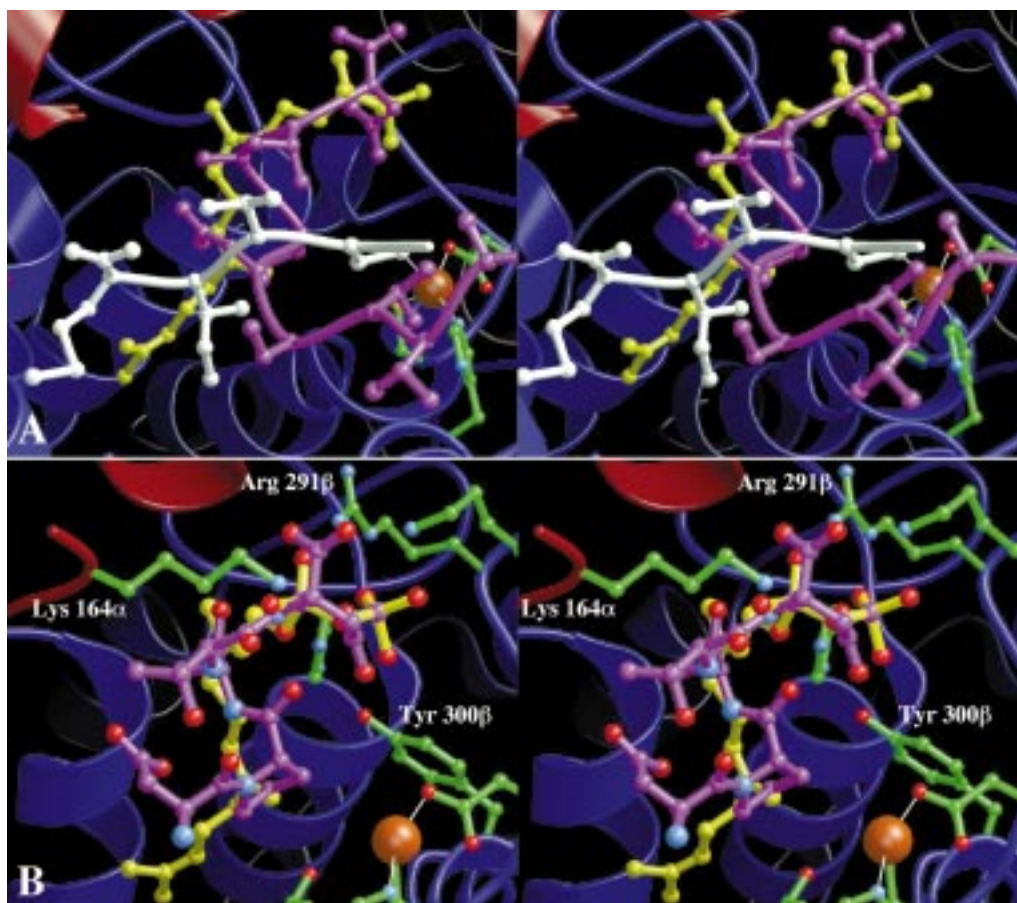
FIGURE 8: Comparisons of FPT structures (a) The interactions made by αHFP (yellow) and the CVIM peptide (white) in the ternary complex are compared to those between FPT molecules related by the crystallographic symmetry present in crystals of unliganded FPT (*17*). In the crystals of unliganded FPT, the C-terminus of the β-subunit (shown in purple) occupies the active site of a symmetry-related molecule. (b) Detailed view of −Pro-Ala-Thr-Asp-COOH, the last four residues of the β-subunit C-terminus (purple), superimposed on the bound conformation of FPP (yellow).

Isoprenoid and Peptide Selectivity. FPT belongs to a family of isoprenoid transferases which includes the highly homologous geranylgeranyl protein transferase I (GGPT-I). The α-subunits of the FPT and GGPT-I heterodimers are identical. Structural similarity between these isoprenoid transferases extends to the β-subunits which exhibit ∼30% amino acid identity (*33*). Unlike FPT for which the 15-carbon farnesyl diphosphate serves as substrate, the GGPT-I substrate is the longer 20 carbon geranylgeranyl diphosphate (GGPP). The ability of these highly homologous enzymes to differentiate between FPP and GGPP has been postulated to involve residues which alter the depth of the isoprenoid binding pocket (*17*). Aspects of the "molecular ruler" hypothesis appear consistent with both the low-resolution structure of an FPP:FPT complex (*29*) and the high-resolution ternary structure reported here.

Comparison of the active sites of FPT and GGPT-I, taken from alignment of the GGPT-I sequence and the structures of FPT, reveals that 14 of the 16 residues involved in FPP binding are identical in the two enzymes (Figure 7). Residues interacting with the diphosphate are strictly conserved, while two residues involved in isoprenoid-binding are different. Substitution of residues with smaller side chains at both nonconserved positions in GGPT-I results in a larger isoprenoid binding pocket. Tyr251β, which packs against the first isoprenoid unit of αHFP in FPT, is a smaller serine residue in GGPT-I. Similarly, the side chain of

Trp102β which packs adjacent to the third isoprenoid unit in FPT is a threonine in GGPT-I (Figure 7). Removal of both aromatic rings could both provide additional space for the extra five carbons needed to accommodate GGPP in GGPT-I and decrease the affinity of GGPT-I for FPP owing to the loss of hydrophobic contacts. Given that the isoprenoid contacts the bound peptide, alteration in side-chain composition and possibly the bound conformation of GGPT-I peptide substrates could also change the size of the isoprenoid binding pocket.

Isoprenoid Mimicking Peptides. The structural results suggest potential binding modes for peptidic inhibitors competitive with FPP. Several have been discovered and one of the most potent is D-tryptophan-D-methionine-D-4-chlorophenylalanine-L-γ-carboxyglutamic acid ($K_i = 2$ nM) (*8*). In the first crystal form of FPT (*17*), the active site was occupied by 10 carboxy terminal residues of the β-subunit of a symmetry-related molecule. It was initially proposed that the C-terminus, with the sequence DLTSD-PATD-COOH, mimicked features of the bound CaaX substrate (*17*). However, the structure reported here reveals that the last four residues of the β-subunit, −Pro-Ala-Thr-Asp-COOH, actually occupy the FPP-binding site (Figure 8b). The negatively charged carboxy terminus and aspartic acid side chain form electrostatic interactions within the FPP diphosphate site. The Ala side-chain methyl binds in the hydrophobic pocket occupied by the first isoprenoid unit,
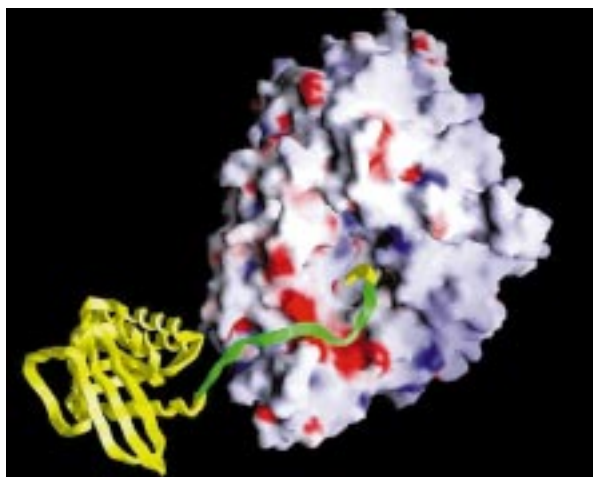
FIGURE 9: Model of K-Ras bound to FPT. The GRASP (*28*) calculated surface of FPT is shown with the regions of positive and negative electrostatic potential colored blue and red, respectively. The conformation of CVIM corresponding to the ras C-terminal CaaX sequence (residues 185−188) and the crystal structure of the GTP binding domain of H-Ras [residues 1−166, PDB code 5p21 (*38*)] are shown as yellow ribbons. The intervening sequence comprising residues 167−184 was sufficiently flexible to place the basic poly-lysine region characteristic of K-Ras close to a prominent electronegative region near the active site.

and the Pro pyrrolidine ring is situated in the second isoprenoid binding pocket. Residues Thr-Ser-Asp of the β-subunit do indeed overlap the Ca_1a_2X peptide binding site, but the main-chain and side-chain orientations are very different (Figure 8a).

Conformation of Bound Peptides. The structure reported here provides the first crystallographic view of FPT complexed with a substrate peptide. The CVIM binds in an extended conformation and packs adjacent to both FPT and the FPP analogue. The cysteine sulfur of the peptide is liganded to the active-site zinc. Unlike polypeptide recognition by serine proteases where the substrate backbone is extensively hydrogen bonded to the protease, only one substrate-to-enzyme backbone hydrogen bond forms in the FPT:peptide complex. Lack of a well-defined register of substrate amino acids with the FPT backbone, as for serine proteases, raises the possibility that while the cysteine sulfur ligation to the zinc is conserved, the overall conformation of the Ca_1a_2X backbone may vary with amino acid sequence. The peptide substrate used in the studies presented here, CVIM, corresponds to the Ca_1a_2X sequence of K-Ras 4a and K-Ras 4b isoforms. Substrates with alternate termini such as H-ras, mating factor a, and retinal cGMP phosphodiesterase which terminate in Ser, Ala, and Gln, respectively, may bind differently (*6*).

Evidence that other sequences, including Ca_1a_2X motifs, exhibit alternate binding modes comes from crystallographic and NMR experiments. In the first crystal structure of FPT (*17*), a portion of the β-subunit was located in the active site. As described above, the carboxy terminal seven residues occupy both the isoprenoid and Ca_1a_2X-binding pocket and do not mimic the CVIM peptide conformation. NMR structures of peptides bound to FPT showed intrapeptide hydrogen bonds. In the absence of isoprenoid, the last seven residues of K-Ras 4b, KTKCVFM, adopted a type I β-turn (*34*). A type III β-turn was observed for inhibitory peptide CVWM in the presence of FPT and αHFP (*35*).

FPT:p21Ras:FPP Complex. The 188 or 189 residue H-Ras, N-Ras, and K-Ras proteins are the FPT substrates in vivo. In solution, H-Ras is a two domain molecule with the 166 amino terminal residues folded into a compact GTP binding domain while the carboxy terminal 23 residues bearing the Ca_1a_2X sequence are unordered. The structure reported here clearly shows that the Ca_1a_2X sequence becomes ordered within the FPT active-site cavity. In a model of the full-length Ras:FPT complex (Figure 9), only a few additional residues would be required to link the Ca_1a_2X sequence to the Ras GTP-binding domain. The structure of the Ca_1a_2X peptide complexed with FPT clearly demonstrates that the entire 20 residue carboxy terminus of Ras is not required to make the Ca_1a_2X sequence accessible to the FPT active site.

The amino acids between the GTP-binding domain and the Ca_1a_2X sequence influence the relative farnesylation rates of Ras isoforms. Experiments with full-length Ras and Ras-derived peptides demonstrated that seven lysine residues located within the sequence 175−182 contribute to the increased affinity of FPT for the Ki-Ras4B isoform (*36, 37*). Favorable surface interactions between Ki-Ras4B and FPT may contribute to an increase in FPT k_{cat} for Ki-Ras4B (*36, 37*). In the model of the Ras:FPT complex (Figure 9), the lysine side chains of Ki-Ras4B are positioned to interact with negatively charged residues on the surface of the FPT α-subunit (Asp59, Glu114, Glu125, Asp147, Glu150, Glu151, and Glu161) and several residues in the β-subunit (Asp91, Glu94, and Asp97).

ACKNOWLEDGMENT

REFERENCES

1. Casey, P., Solski, P., Der, C., and Buss, J. (1989) *Proc. Natl. Acad. Sci. U.S.A. 86*, 8323−8327.
2. Powers, S., Michaelis, S., Broek, D., Santa, A., Field, J., Herskowitz, I., and Wigler, M. (1986) *Cell 47*, 413−422.
3. Cox, A., and Der, C. (1997) *Biochim. Biophys. Acta 1333*, F51−F71.
4. Willumsen, B., Christensen, A., Hubert, N., Papageorge, A., and Lowy, D. (1984) *Nature 310*, 583−586.
5. James, G., Goldstein, J., Brown, M., Rawson, T., Somers, T., McDowell, R., Crowley, C., Lucas, B., Levinson, A., and Marsters, J. (1993) *Science 260*, 1937−1942.
6. Reiss, Y., Stradley, S., Gierasch, L., Brown, M., and Goldstein, J. (1991) *Proc. Natl. Acad. Sci. U.S.A. 88*, 732−736.
7. Goldstein, J., Brown, M., Stradley, S., Reiss, Y., and Gierasch, L. (1991) *J. Biol. Chem. 266*, 15575−15578.
8. Wallace, A., Koblan, K., Hamilton, K., Marquis-Omer, D., Miller, P., Mosser, S., Omer, C., Schaber, M., Cortese, R., Oliff, A., Gibbs, J., and Pessi, A. (1996) *J. Biol. Chem. 271*, 31306−31311.
9. Pompliano, D., Rands, E., Schaber, M., Mosser, S., Anthony, N., and Gibbs, J. (1992) *Biochemistry 31*, 3800−3807.
10. Pompliano, D., Schaber, M., Mosser, S., Omer, C., Shafer, J., and Gibbs, J. (1993) *Biochemistry 32*, 8341−8347.
11. Furfine, E., Leban, J., Landavazo, A., Moomaw, J., and Casey, P. (1995) *Biochemistry 34*, 6857−6862.
12. Fu, H., Beese, L., and Casey, P. (1998) *Biochemistry 37*, 4465−4472.
13. Huang, C., Casey, P., and Fierke, C. (1997) *J. Biol. Chem. 272*, 20−23.
14. Mu, Y., Omer, C., and Gibbs, R. (1996) *J. Am. Chem. Soc. 118*, 1817−1823.

15. Cassidy, P., and Poulter, C. (1996) *J. Am. Chem. Soc. 118*, 8761−8762.

16. Dolence, J., and Poulter, C. (1995) *Proc. Natl. Acad. Sci. U.S.A. 92*, 5008−5011.

17. Park, H., Boduluri, S., Moomaw, J., Casey, P., and Beese, L. (1997) *Science 275*, 1800−1804.

18. Bishop, W., Bond, R., Petrin, J., Wang, L., Patton, R., Doll, R., Njoroge, G., Catino, J., Schwartz, J., Windsor, W., Syto, R., Schwartz, J., Carr, D., James, L., and Kirschmeier, P. (1995) *J. Biol. Chem. 270*, 30611−30618.

19. Jancarik, J., and Kim, S.-H. (1991) *J. Appl. Crystallogr. 24*, 409−411.

20. Cox, M., and Weber, P. (1988) *J. Cryst. Growth 90*, 318−324.

21. Otwinowski, Z., and Minor, W. (1997) in *Methods in Enzymology* (Carter, C., and Sweet, R., Eds.) pp 307−326, Academic Press, New York.

22. Brünger, A., Kuriyan, J., and Karplus, M. (1987) *Science 235*, 458−460.

23. Brünger, A. (1990) *Acta Crystallogr., Sect. A 46*, 46−57.

24. Sack, J. (1988) *J. Mol. Graphics 6*, 224−225.

25. Chothia, C., and Lesk, A. (1986) *EMBO J. 5*, 823−826.

26. Kraulis, P. (1991) *J. Appl. Crystallogr. 24*, 946−950.

27. Merritt, E. A., and Murphy, M. E. P. (1994) *Acta Crystallogr., Sect. D 50*, 869−873.

28. Nicholls, A., Sharp, K., and Honig, B. (1991) *Proteins: Struct., Funct., Genet. 11*, 281.

29. Long, S., Casey, P., and Beese, L. (1998) *Biochemistry*, *37*, 9612−9618.

30. Kral, A., Diehl, R., deSolms, S., Williams, T., Kohl, N., and Omer, C. (1997) *J. Biol. Chem. 272*, 27319−27323.

31. Bernstein, F., Koetzle, T., Williams, G., Meyer, E., Brice, M., Rodgers, J., Kennard, O., Shimanouchi, T., and Tasumi, M. (1977) *J. Mol. Biol. 112*, 535−542.

32. Cane, D., Chiu, H., Lang, P., and Anderson, K. (1997) *Biochemistry 36*, 8332−8339.

33. Seabra, M., Reiss, Y., Casey, P., Brown, M., and Goldstein, J. (1991) *Cell 65*, 429−434.

34. Stradley, S., Riza, J., and Gierasch, L. (1993) *Biochemistry 32*, 12586−12590.

35. Koblan, K., Culberson, J., Desolms, S., Giuliani, E., Mosser, S., Omer, C., Pitzenberger, S., and Bogusky, M. (1995) *Protein Sci. 4*, 681−688.

36. Zhang, F., Kirschmeier, P., Carr, D., James, L., Bond, R., Wang, L., Patton, R., Windsor, W., Syto, R., Zhang, R., and Bishop, W. (1997) *J. Biol. Chem. 272*, 10232−10239.

37. James, G., Goldstein, J., and Brown, M. (1995) *J. Biol. Chem. 270*, 6221−6226.

38. Pai, E., Krengel, U., Petsko, G., Goody, R., Kabsch, W., and Wittinghofer, A. (1990) *EMBO J. 9*, 2351−2359.